Research Article

Nano Research
2021, 14(11): 4116–4124

ISSN 1998-0124 CN 11-5974/O4
https://doi.org/10.1007/s12274-021-3351-x

Crystalline all-inorganic lead-free $Cs_3Sb_2I_9$ perovskite microplates with ultra-fast photoconductive response and robust thermal stability

Sujit Kumer Shil[1,3,§], Fei Wang[2,4,5,§] (✉), Zhengxun Lai[2], You Meng[2], Yunpeng Wang[4], Dongxu Zhao[4], Mohammad Kamal Hossain[1,6], Kingsley O. Egbo[1], Ying Wang[1], Kin Man Yu[1] (✉), and Johnny C. Ho[2,5] (✉)

[1] *Department of Physics, City University of Hong Kong, Kowloon, Hong Kong, China*
[2] *Department of Materials Science and Engineering, City University of Hong Kong, Kowloon, Hong Kong, China*
[3] *Department of Physics, Khulna University of Engineering & Technology (KUET), Khulna 9203, Bangladesh*
[4] *State Key Laboratory of Luminescence and Applications, Changchun Institute of Optics, Fine Mechanics and Physics, Chinese Academy of Sciences, 3888 Dongnanhu Road, Changchun 130021, China*
[5] *State Key Laboratory of Terahertz and Millimeter Waves, City University of Hong Kong, Kowloon, Hong Kong, China*
[6] *Department of Physics, Comilla University, Kotbari, Comilla 3506, Bangladesh*
[§] *Sujit Kumer Shil and Fei Wang contributed equally to this work.*

Received: 21 October 2020 / **Revised:** 16 January 2021 / **Accepted:** 20 January 2021

ABSTRACT

Hybrid organolead halide perovskites have attracted tremendous attention due to their recent success as high efficiency solar cell materials and their fascinating material properties uniquely suitable for optoelectronic devices. However, the poor ambient and operational stability as well as the concern of lead toxicity greatly hamper their practical utilization. In this work, crystalline, all-inorganic and lead-free $Cs_3Sb_2I_9$ perovskite microplates are successfully synthesized by a two-step chemical vapor deposition method. As compared with other typical lead-free perovskite materials, the $Cs_3Sb_2I_9$ microplates demonstrate excellent optoelectronic properties, including substantial enhancements in the Stokes shift, exciton binding energy and electron-phonon coupling. Simple photoconductive devices fabricated using these microplates exhibit an ultra-fast response with the rise and decay time constants down to 96 and 58 μs, respectively. This respectable photoconductor performance can be regarded as a record among all the lead-free perovskite materials. Importantly, these photodetectors show superior thermal stability in a wide temperature range, capable to function reversibly between 80 and 380 K, indicating their robustness to operate under both low and high temperatures. All these results evidently suggest the technological potential of inorganic lead-free $Cs_3Sb_2I_9$ perovskite microplates for next-generation high-performance optoelectronic devices.

KEYWORDS

all-inorganic, lead-free perovskites, $Cs_3Sb_2I_9$, microplates, photoresponse, stability

1 Introduction

In past decades, photodetectors have been developed into one of mature technological products for the conversion of incident optical information into electrical signals [1, 2]. They are not only essential devices in conventional technologies, including communication, imaging, environmental monitoring and target detection, but also have a huge application potential in emerging areas, such as object recognition for self-driving vehicles, artificial intelligence and internet-of-things systems [2, 3]. The recent advent of hybrid organolead halide perovskites (ABX_3 with A = organic cation, B = Pb and X = halide) as materials with properties uniquely suitable for high efficiency solar cells and many optoelectronic devices [4–13] provides the opportunity to further enhance the performance of photodetectors using halide perovskites. For instance, using solution-processed $CH_3NH_3PbI_3$ films as device channels, Hu et al. fabricated broadband photodetectors (from ultraviolet to visible) with the photoresponsivity of 3.49 A/W, 0.0367 A/W and external quantum efficiency of 1.19×10^3%, 5.84% at 365 nm and 780 nm irradiation wavelength, respectively [6]. Dou and his team later demonstrated another high-performance photodetector utilizing $CH_3NH_3PbI_{3-x}Cl_x$ films, covering a linear dynamic range over 100 decibels (dB), with an enhanced detectivity up to 10^{14} Jones and fast photoresponse with 3-dB bandwidth approaching 3 MHz [7]. These examples demonstrated that symmetrically structured photoconductive detectors with the excellent performance could be achieved using organometal halide perovskites [14].

Although the detectivity and responsivity of hybrid perovskite photodetectors are superior to other photodetectors, they tend to be unstable during long term operation in ambient air and temperature [15–17]. These instabilities are mostly attributed to the low thermal decomposition temperature and extreme sensibility of organic cations (A) to moisture [18–21]. At the same time, the concern of the toxicity of Pb would inevitably

Address correspondence to Fei Wang, wangf@ciomp.ac.cn; Kin Man Yu, kinmanyu@cityu.edu.hk; Johnny C. Ho, johnnyho@cityu.edu.hk

limit these Pb-based perovskites for practical utilization. Hence, there has been an extensive search for environmental-friendly lead-free all-inorganic perovskites for photodetector fabrication with the aims to improve both device stability as well as performance [22–24]. Typically, the unstable organic cation group can be replaced by a monovalent metal cation (e.g. Cs^+ or Rb^+). However, choices of non-toxic B ions to replace Pb are severely limited by the narrow range of the Goldschmidt tolerance factor for a closed packed perovskite structure [25, 26]. With the similar atomic radius of Pb, Sn has been once considered as the promising alternative for Pb-free perovskites [27–29] but the rapid oxidation of Sn^{2+} to Sn^{4+} makes the Sn-based perovskites very unstable in ambient. Lately, there is a new class of defect-ordered perovskites with exceptional stability with the structure of $A_3M_2X_9$ that can be derived by replacing a portion of the metal sites of conventional ABX_3 perovskites by vacancies. Here, M denotes Bi^{3+} or Sb^{3+} ions occupying 2/3 of the B sites in ABX_3 perovskites [5, 30–33]. In particular, solution-processed $Cs_3Sb_2I_9$ perovskite thin films have been explored for light emitting [34, 35] and photovoltaic applications [32, 36, 37]. However, due to the poor crystallinity and high trap-state density in solution-processed materials, the device performance of $Cs_3Sb_2I_9$ based optoelectronic devices are far from acceptable [5, 30, 38]. Although solution process is a facile and common way to fabricate perovskite materials, the different solubilities of precursors in solvents make them hard to react proportionally and uniformly, hindering the obtained crystallinity of the reaction products. As compared with the solution-processed materials, chemical vapor deposition (CVD) is a well-established method to achieve excellent optoelectronic materials, especially for micro- and nanostructures with improved surface-to-volume ratio for the better photodetector performance. However, due to the extreme disparity in the melting temperature for CsI (621 °C) and SbI_3 (171 °C), synthesis of high-quality $Cs_3Sb_2I_9$ materials using the CVD process is a formidable task.

In this work, in order to overcome the challenges growing high quality $Cs_3Sb_2I_9$ by conventional CVD method, we developed a two-step CVD process and successfully synthesized highly-crystalline, all-inorganic and Pb-free $Cs_3Sb_2I_9$ microplates. The $Cs_3Sb_2I_9$ microplates exhibit substantial enhancements in the Stokes shift, exciton binding energy and electron-phonon coupling over other perovskite structures. Photoconductive devices fabricated using these $Cs_3Sb_2I_9$ microplates deliver a respectable performance with responsivity up to 40 mA/W and on/off current ratio reaching 10^4 at 532 nm irradiation wavelength. More importantly, their rise and decay time constants can be down to 96 and 58 μs, respectively, constituting a record fast response among all Pb-free perovskite photoconductive devices. These $Cs_3Sb_2I_9$ microplate devices also demonstrated superior thermal stability within a wide temperature range, spanning reversibly from 80 K all the way to 380 K. All these results evidently provide a simple but effective way to achieve crystalline, all-inorganic and lead-free perovskites for high-performance and robust optoelectronic devices.

2 Results and discussion

$Cs_3Sb_2I_9$ perovskite microplates were grown in a single zone tube furnace by using a two-step CVD approach. The schematic of the overall synthesis strategy of $Cs_3Sb_2I_9$ perovskite microplates is illustrated in Fig. S1(a) in the Electronic Supplementary Material (ESM). The process details are described in the Method section, while the microplate evolution is investigated by scanning electron microscopy (SEM) after each process step as depicted in Figs. S1(b)–S1(d) in the ESM. To be specific, the optimized CsI films were first grown on Si substrates in step-I (Fig. S1(b) in the ESM). Then, the SbI_3 precursor layer was deposited over the CsI film for the subsequent formation of microplates in step-II (Fig. S1(c) in the ESM). Since the melting temperature of CsI is relatively high (621 °C), the deposition of SbI_3 precursor on the CsI film at a much lower temperature (130 °C) would simply make the crystallization reaction process more uniform and stoichiometric. The uniform crystallization process induces the formation of SbI_3 microplates, instead of continuous SbI_3 films, without deteriorating the material quality of the underlying CsI film. An SEM image of SbI_3 microplates grown directly on the sapphire substrate under the same condition is given in Fig. S2 in the ESM. The same SbI_3 microplate morphology obtained shows that the as-prepared CsI film does not affect the deposition of the SbI_3 precursor. After the two-step deposition, the sample was annealed at 180 °C in the tube furnace in flowing N_2. During the annealing process, due to the lower melting point of SbI_3, the SbI_3 microplates would function as precursor sources to react with the CsI film. After the recrystallization, $Cs_3Sb_2I_9$ perovskite microplates with a hexagonal shape were achieved on the substrate (Fig. 1(a) and Fig. S1(d) in the ESM), showing the homogeneous distribution of crystal morphologies and sizes. We note that the $Cs_3Sb_2I_9$ microplates were not defined or inherited from the SbI_3 microplates, and the edge lengths of the microplates are 5 to 10 μm. This two-step CVD method can provide a simple and effective way to synthesize large-scale perovskite microplates for the subsequent device fabrications.

The crystal structure and chemical composition of the obtained perovskite microplates were first characterized. Detailed crystallographic data are given in Table S1 in the ESM and the unit cell and 2D layered structure of $Cs_3Sb_2I_9$ perovskite are shown schematically in Fig. 1(b) and Fig. S3 in the ESM. The $Cs_3Sb_2I_9$ perovskite consists of bi-octahedral $(Sb_2I_9)^{3-}$ clusters that are surrounded by Cs cations to achieve the charge balance. The unit cell has a trigonal phase with the space group of $P\bar{3}m1$ (164) with lattice parameters of $a = b =$ 8.42 Å, $c = 10.386$ Å, and angles of $\alpha = \beta = 90°$, $\gamma = 120°$. X-ray diffraction (XRD) measurements (Fig. 2) reveal the crystalline nature of the $Cs_3Sb_2I_9$ perovskite microplates, with diffraction peaks indexed to the 2D layered $Cs_3Sb_2I_9$ perovskite structure (JCPDS No. 88-0690). Even after one-month ambient exposure

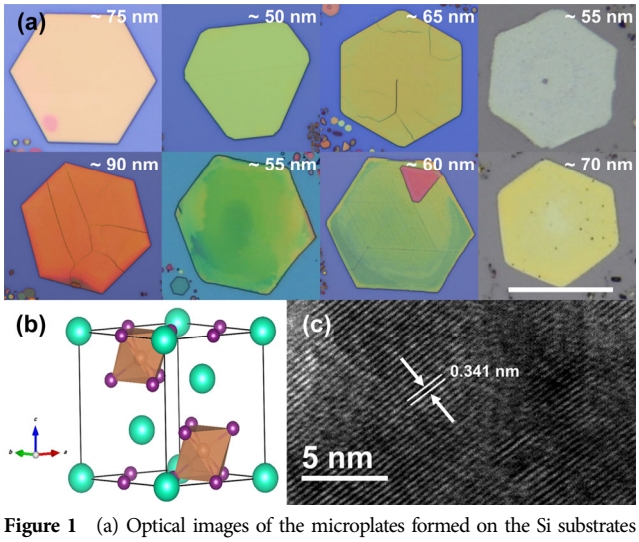

Figure 1 (a) Optical images of the microplates formed on the Si substrates (coated by 250 nm SiO_2, purple background) and sapphire substrates (gray background), showing the homogeneous distribution of crystal morphologies and sizes. The different colors of the microplates are originated from their different thicknesses. Scale bars are 10 μm. (b) An illustration of the atomic model of a $Cs_3Sb_2I_9$ unit cell. (c) A HRTEM image of the microplate.

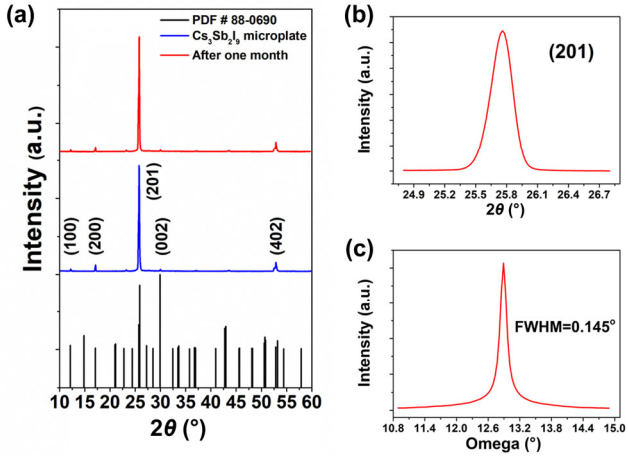

Figure 2 XRD patterns (a), high-resolution XRD spectrum (b) and the corresponding rocking curve (c) of the microplates.

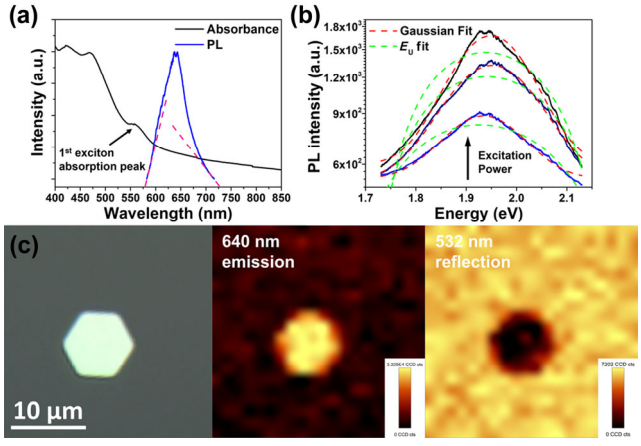

Figure 3 (a) UV–vis absorption and steady-state PL spectra of the $Cs_3Sb_2I_9$ microplates. (b) PL spectra under different exciting powers ($\lambda_{excitation}$ = 532 nm) and corresponding fitted curves. (c) Steady-state PL mapping of a typical $Cs_3Sb_2I_9$ microplate.

without any capsulation (temperature: ~ 26 °C, humidity: 60%–70%), the XRD pattern does not show any noticeable change, indicating the excellent stability of these microplates in oxygen and moisture environment at room temperature (Fig. 2(a)). High-resolution XRD of the (201) peak (Fig. 2(b)) shows that the (201) peak is rather sharp and symmetric without any shoulders, indicating the good phase purity of the $Cs_3Sb_2I_9$ microplates. The corresponding rocking curve (Fig. 2(c)) further reveals a relatively narrow full-width-half-maximum (FWHM) of 0.145°, which confirms the excellent crystallinity of the microplates. Also, Fig. S4 in the ESM presents the XRD patterns of precursor layers (CsI only and SbI_3 only) grown under the same CVD condition mentioned above. They don't share any peaks with the patterns in Fig. 2(a), indicating the absence of impurities and residual raw materials in the $Cs_3Sb_2I_9$ microplates.

The highly crystalline nature of the microplates is further confirmed by the high-resolution transmission electron microscopy (HRTEM) image of the sample (Fig. 1(c)) which clearly shows lattice fringes with a spacing of 0.341 nm, corresponding to the (201) plane of the $Cs_3Sb_2I_9$ crystal. The thickness of the microplates was studied by atomic force microscopy (AFM), which shows a distribution of thicknesses between 50 to 100 nm (Fig. S5 in the ESM). In addition, the elemental composition of these $Cs_3Sb_2I_9$ microplates was analyzed by using energy dispersive X-ray spectroscopy (EDX). In the EDX spectrum from a microplate, strong signals from Cs, Sb and I with the atomic ratios (%) of Cs:Sb:I = 22.1:15.7:62.2 are observed, consistent with the expected stoichiometric ratio of $Cs_3Sb_2I_9$ perovskite (Fig. S6 in the ESM). Notably, these microplates have a relatively uniform distribution of their constituents as supported by the corresponding elemental mappings (Fig. S7 in the ESM). All these results confirm the crystallinity, crystal phase-purity and chemical stoichiometry of $Cs_3Sb_2I_9$ perovskite microplates grown by the two-step CVD process.

UV–vis absorption and photoluminescence (PL) measurements were carried out to examine the bandgap and luminescent characteristics of $Cs_3Sb_2I_9$ perovskite microplates. Based on the absorption spectrum, there is an absorption peak located at 556 nm, which can be considered as the 1st exciton absorption peak (Fig. 3(a)). This exciton peak is then followed by an absorption edge, attributed to the band-to-band photon absorption. Using the Tauc plot, a bandgap energy of 2.24 eV can be determined for these perovskite microplates (Fig. S8 in the ESM). An exciton binding energy of ~ 230 meV can be estimated from the edges of the bandgap and exciton absorption. Meanwhile, by fitting the absorption spectrum with the quantum-well absorption model modified for nanoplates or nanosheets [39, 40], we obtain an exciton binding energy of 282 meV (fitting method and results shown in Fig. S9 in the ESM), in good agreement with the experimental value determined above. This exciton binding energy for $Cs_3Sb_2I_9$ microplates is slightly lower than that reported for Bi-based perovskites (e.g. $A_3Bi_2I_9$ with the energy value of 300–400 meV) [38, 41], but much higher than those for Pb-based perovskites and other semiconductor materials. Devices fabricated from materials with high exciton binding energy can maintain good device performance under large electric fields, high temperature and intense irradiation conditions. Hence, the high exciton binding energy of $Cs_3Sb_2I_9$ microplates suggests that they are potential candidates for optoelectronic devices operating in harsh environments. Moreover, the PL peak of the microplates is found to locate at 640 nm, whereas the peak sharpness indicates the good crystallinity of the samples. In this case, there is a strong Stokes shift of approximately 520 meV between the absorption edge and the PL emission. This Stokes shift value is much higher than other semiconductor materials [42, 43]. In contrast, typical lead halide perovskites have the small Stokes shift (30–70 meV) which gives rise to a strong self-absorption effect [42, 44], severely restricting their light outcoupling efficiency [42]. The relatively large Stokes shift of the $Cs_3Sb_2I_9$ microplates would make them as attractive active materials for high-performance light emitting and laser diodes. Notably, copper-based halides perovskites have even the larger exciton binding energies (335–490 meV for $Cs_3Cu_2I_5$ [45, 46]; ~ 205 meV for $CsCu_2I_3$ [47, 48] and ~ 700 meV for Ru_2CuBr_3 [42]) and Stokes shifts (161–238 nm for $Cs_3Cu_2I_5$; ~ 210 nm for $CsCu_2I_3$ and ~ 85 nm for Ru_2CuBr_3, respectively). Benefitting from the small self-absorption and efficient light out-coupling, high radioluminescence yields were observed within these materials [42, 45–48]. However, such large exciton binding energy could also lead to the difficulty of exciton dissociation in the materials, which generally result in a higher dark current and lower light current [49, 50]. Therefore, for achieving high-performance photon-electron conversion devices operating under high temperatures, materials with a moderate exciton binding energy is more desirable.

It is also worth noting that the PL emission peak of the $Cs_3Sb_2I_9$ microplates has an asymmetrical shape, with the slope of the peak at the low-energy (longer wavelength) side being much smaller than that of the high-energy (shorter wavelength) side (Fig. 3(a)). This asymmetry of the peak shape

can reflect the skewness and fluctuation of local potentials in the crystal, which suggests the presence of a strong electron-phonon coupling. Technically, a strong electron-phonon coupling in materials would lead to the charge localization and emission of phonons, followed by the altered energy of emitted photons [51]. In this manner, the low-energy tail of the PL peak observed for $Cs_3Sb_2I_9$ microplates is an indication of electron-phonon couplings in the material. In order to further evaluate electron-phonon couplings in these $Cs_3Sb_2I_9$ microplates, we use the theory of Toyozawa [51, 52], in which the PL peak width, $W(T)$, was related to the average phonon energy, electron-photon coupling and other parameters via the following expressions

$$W(T) = 2.36\sqrt{S}E_{Ph}\left[\coth\left(\frac{E_{Ph}}{2k_BT}\right)\right]^{\frac{1}{2}} \quad (1)$$

$$S = \frac{W(T)^2}{5.5696{E_{Ph}}^2\coth\left(\frac{E_{Ph}}{2k_BT}\right)} \quad (2)$$

where S is the Huang–Rhys electron–phonon coupling parameter, k_B is the Boltzmann constant, T is the temperature and E_{Ph} is the effective phonon energy. The E_{Ph} value of $Cs_3Sb_2I_9$ materials is calculated to be 7.0 ± 0.8 meV [51]. PL measurements were performed on $Cs_3Sb_2I_9$ microplates with increasing excitation power densities (Fig. 3(b)) and the PL spectra were analyzed using Eqs. (1) and (2). Best fits with Gaussian functions of the spectra reveals a $W(T)$ = 0.19 ± 0.014 eV at 300 K for the $Cs_3Sb_2I_9$ microplates, giving rise to an S parameter of 17.88 ± 5.0. This S parameter value is higher than the reported value for CsX (e.g. 4.8, 3.7 and 12 for Cl, Br and I, respectively) [53, 54], demonstrating the much stronger electron-phonon coupling of the $Cs_3Sb_2I_9$ microplates. Furthermore, there is also an exponential tail at the lower energy side of the absorption spectrum. This tail is known as Urbach tail that is resulted from the intrinsic electron-phonon coupling [55, 56]. The value of Urbach energy, E_U, can be estimated by the van Roosbroeck-Shockley relationship [56, 57]

$$\alpha(E,T) \propto \exp\left(\frac{E}{E_U}\right) \quad (3)$$

$$I_{PL}(E,T) \propto \alpha(E,T)E^2\exp\left(\frac{E}{-k_BT}\right) \quad (4)$$

where $I_{PL}(E, T)$ and $\alpha(E, T)$ are the PL and absorption spectra, respectively. The relationship between $I_{PL}(E, T)$ and E_U can then be described in the following expression

$$I_{PL}(E,T) = AE^2\exp\left(\frac{E}{E_U} - \frac{E}{k_BT}\right) \quad (5)$$

where A is a constant. By fitting the experimental spectra with Eq. (5), the E_U value is estimated to be 26.5 ± 0.005 meV, which is much higher than that for $CsPbBr_3$ (14 meV), $MAPbBr_3$ (15 meV) and $FAPbBr_3$ (17 meV) [56]. This further confirms the stronger electron-phonon coupling of the $Cs_3Sb_2I_9$ microplates, which gives rise to the electric dipole moments, the coupling to the electric field of plasmons and the longitudinal collective excitations of electron gas [58].

Furthermore, PL mapping of the $Cs_3Sb_2I_9$ microplates was also performed. As observed in the mapping of a typical microplate shown in Fig. 3(c), PL emission mainly occurs from the hexagonal $Cs_3Sb_2I_9$ microplate, with stronger intensities from the inner region of microplate than the edges and corner regions of the hexagon (Fig. S10 in the ESM). This spatial intensity variation is possibly caused by the relatively low specific surface area and low surface defect density of the microplate. Moreover, the low reflection of the exciting beam from the hexagonal plate also indicates the good absorbance of the $Cs_3Sb_2I_9$ microplate. The charge recombination properties of the microplates are revealed by time-resolved PL measurements. As shown in Fig. S11 in the ESM, the PL decay curve can be well fitted by a bi-exponential decay model with a short lifetime (τ_1) of 5.9 ns and a long lifetime (τ_2) of 24.3 ns, respectively. The fast decay rate of PL intensity indicates that the faster exciton recombination dominates over the slower transitions at defect states [35]. These findings illustrate the excellent optical properties of $Cs_3Sb_2I_9$ microplates, making them uniquely suitable for various optoelectronic devices.

To demonstrate the practical utilization of these $Cs_3Sb_2I_9$ microplates, we fabricate simple photoconductive devices and performed detailed performance evaluation studies on these devices. Figure 4(a) shows a schematic diagram of the microplate photodetector with thermally evaporated Au electrodes deposited 10 μm apart on the microplate by using Ni grids (300 mesh) as shadow masks. Before performing any device measurement, the valence band maximum of $Cs_3Sb_2I_9$ was measured by ultraviolet photoelectron spectroscopy (UPS) to be 5.27 eV (Fig. 4(b)). The corresponding energy band alignment of the $Cs_3Sb_2I_9$ microplate photodetector is shown in Fig. 4(c), suggesting that Au with a typical work function of 5.1 eV is an appropriate metal to serve as efficient electrical contacts for the photodetector. The Hall mobility of the $Cs_3Sb_2I_9$ material is ~ 33 $cm^2/(V{\cdot}s)$ with the p-type conductivity, while the tested carrier density is found to be ~ 4×10^{13} cm^{-3}. Then, the current–voltage (I–V) characteristics of $Cs_3Sb_2I_9$ microplate devices were measured to reveal their electrical properties. Figures 4(d) and 4(e) present the I–V curves of the device in the dark and under 532 nm light illumination with increasing power densities. It is seen that the microplate device has a high resistance with a dark current of around several pA in the dark. Yet, under illumination, the output current increases by several orders of magnitude. Also, the linear I–V curves imply that there is an ohmic-like contact formed between Au electrodes and $Cs_3Sb_2I_9$ channels, whereas the increase of current indicates the device being sensitive to incident 532 nm photons. Figure 4(f) shows the successive on/off switching characteristics of the device at 1 V bias upon 532 nm light illumination. At the very instant of illumination, the current increases rapidly over 3 orders of magnitude without any noticeable degradation over repeated switching cycles. With an applied bias of 0.5 V, the on/off ratio between photo- and dark-current can reach up to 4 orders of magnitude (Fig. S12 in the ESM). However, the device dark current at 0.5 V bias increases slowly after several on/off cycles. For stable performance, the optimized operating bias of 1 V is needed for the device.

Since the relationship between photocurrent and light intensity can serve as a direct evidence to assess the performance stability of a photodetector under both weak and strong signals, the photosensitivity dependence of the device on various incident power densities is hence explored. Figure 4(g) shows that the photocurrent rises proportionally with the increasing power intensities from 0 to 47 mW/cm^2 under 532 nm light illumination, which suggests that more incident photons can generate more photo-carriers in the device. As a critical parameter to characterize the performance of photodetectors, the responsivity (R) of the device is defined as

$$R = \frac{I_{ph}}{L_{light}} \quad (6)$$

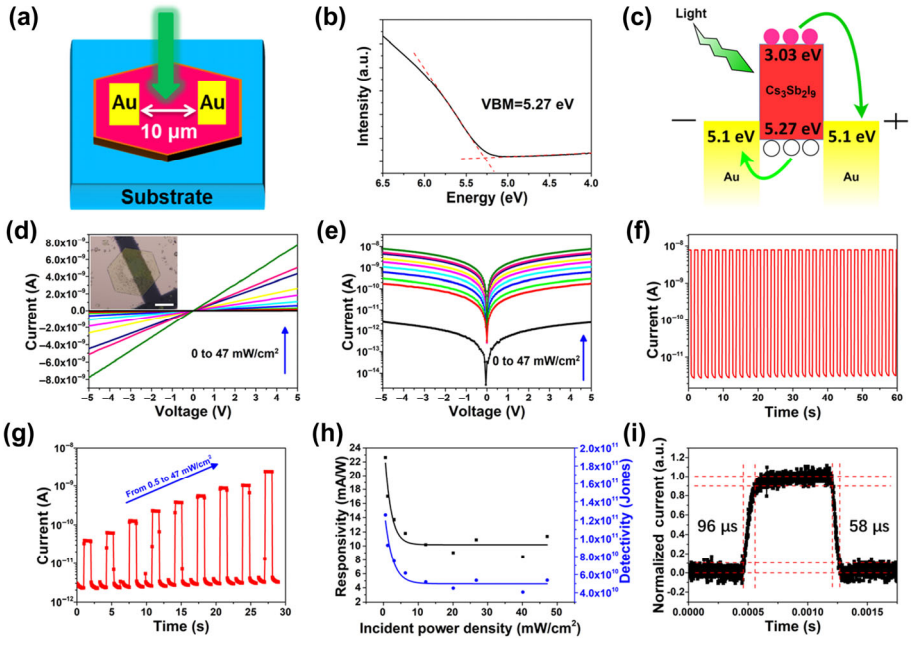

Figure 4 (a) A schematic illustration of the $Cs_3Sb_2I_9$ microplate photodetector. (b) A UPS spectrum showing the valence band maximum (VBM) value of the $Cs_3Sb_2I_9$ microplate. (c) A schematic showing the energy band alignment and light induced carriers transport in the photodetector. ((d) and (e)) *I*–*V* characteristics of the device in the dark and under illumination, respectively. The inset of (d) shows the optical image of the device. The scale bar is 10 μm. (f) The reproducible on/off switching of the device under the incident power density of 47 mW/cm^2. (g) The photocurrent of the device upon various incident power intensities. (h) Power dependent responsivity and detectivity curves of the device. (i) Response of the device to pulsed 532 nm light irradiation at a frequency of 800 Hz under 1 V bias.

where I_{ph} is the photocurrent and L_{light} is the effective power of incident light illuminated on the device. The inset of Fig. 4(d) shows the actual dimension of a typical device and its active area is determined to be 3×10^{-6} cm^2. The responsivity of the device is plotted in Fig. 4(h) as a function of the incident power density. The device responsivity has the highest value of 23 mA/W at a low incident power density of 0.5 mW/cm^2, followed by a rapid decay with the increasing incident power density to a stable value of ~ 10 mA/W for power intensity > 10 mW/cm^2. Because more charge recombination occurs under higher illumination intensity, the lowest-lying trap states with the longest lifetime that provide the highest photoconductive gain at low intensities are filled, resulting in the decrease of the responsivity [59, 60]. As the number of illumination photons increases, the absorption gradually saturates in the microplates. Consequently, the photo-generated carriers and the charge recombination reach a dynamic equilibrium, resulting in the steady value under higher illumination. To further characterize the weakest level of light that the detector can operate, detectivity (D^*) is determined by the responsivity R and the dark current I_D with the following expression

$$D^* = \sqrt{\frac{A}{2qI_D}}R \quad (7)$$

where I_D is the dark current, q is the elementary charge and A is the effective area. Similarly, the maximum detectivity value at the low incident power density of 0.5 mW/cm^2 is found to be 1.26×10^{11} Jones (cm·Hz$^{1/2}$·W^{-1}), which decreases to a stable value of ~ 5×10^{10} Jones at > 10 mW/cm^2 incident power (Fig. 4(h)). Another important parameter characterizing a photodetector is its on/off switching characteristics. The device response time was measured with the 532 nm light source by using a chopper to turn the illumination on and off on the device. The rise time, defined as the time for the current to increase from 10% to 90% of its peak value, is determined to be 96 μs. Likewise, the decay time, described as the time for the current to decrease from 90% to 10% of its peak, is found to be 58 μs. These efficient rise and decay time constants of $Cs_3Sb_2I_9$ microplate devices are already better than other state-of-the-art Pb-free perovskite photodetectors. Performance parameters of photodetectors fabricated from Pb-free perovskite materials reported previously are compiled in Table 1 and compared with our $Cs_3Sb_2I_9$ microplate devices. These rapid response and recovery speeds of the device arises from the fast separation and effective extraction of photo-generated electron-hole pairs in the material, which can be ascribed to the excellent crystal quality of $Cs_3Sb_2I_9$ microplates.

Apart from the response time, it is also essential to evaluate the photoresponse of detectors to different incident wavelengths. As shown in Fig. 5(a), the $Cs_3Sb_2I_9$ microplate device is capable of responding efficiently to the illumination of photons with different wavelengths λ with different photocurrent values. It is clear that the magnitude of photocurrent depends heavily on the light absorption of device active materials. Therefore, we expect to have high photocurrents for above bandgap irradiation with 405 to 532 nm photons. The spectral responsivity curve of the device is measured and illustrated in Fig. 5(b). It is noted that the device maintains a high responsivity with incident photons with λ ranging from 350 to 550 nm, and then the responsivity decreases dramatically for photons with λ > 600 nm. This spectral responsivity follows the absorption characteristics and the exciton absorption edge of $Cs_3Sb_2I_9$ microplates as depicted in Fig. 3(a). The absorption tail which extends from 600 to 800 nm results in a low photocurrent obtained at λ ~ 635 nm (Fig. 5(a)). The spectral range and magnitude of the responsivity curve can be further manipulated by tailoring the optical absorption properties via controlling the composition of the cation and anion halides in all-inorganic lead-free $A_3M_2X_9$ perovskites.

As mentioned earlier, the stability (thermal and ambient) issue of perovskite devices, in particular organic hybrid halide perovskite devices is still a challenging hurdle. In order to examine the thermal stability of $Cs_3Sb_2I_9$ microplate photodetectors, the device performance was investigated in the

Table 1 A comparison of performance parameters of photodetectors fabricated using various Pb-free halide perovskite materials

Material	Method/morphology	Responsivity (mA/W)	Detectivity (Jones)	Highest On/off ratio	Rise/decay time (ms)	Ref.	Date
$CH_3NH_3SnI_3$	CVD/nanowire	470	8.8×10^{10}	N/A	1,500/400	[61]	2017
$CsBi_3I_{10}$	Solution/thin film	21,800	1.93×10^{13}	10^5	0.33/0.38	[23]	2017
$MA_3Sb_2I_9$	Solution/bulk crystal	40,000	10^{12}	10	0.4 /0.9	[5]	2018
$(TMHD)BiBr_5$	Solution/bulk crystal	100	N/A	10^3	8.9/10.2	[62]	2018
$Cs_2AgBiBr_6$	Solution/thin film	7010	5.66×10^{11}	10^4	0.956/0.995	[63]	2018
$Cs_2SnCl_{6-x}Br_x$	Solution/bulk crystal	N/A	2.71×10^{10}	N/A	N/A	[64]	2019
$Cs_3Cu_2I_5$	Solution/thin film	64.9	10^{11}	127	26.2/49.9	[65]	2019
$(PEA)_2SnI_4$	Solution/2D	121	8.09×10^9	10^2	34/38	[66]	2019
$Cs_2AgBiBr_6$	Solution/thin film	1,460	9.4×10^{12}	10^4	3.463/8.442	[67]	2019
$Cs_3Sb_2Br_9$	Solution/nanoflake	3,800	2.6×10^{12}	N/A	48/24	[68]	2019
$Cs_3Bi_2I_9$	Solution/thin film	7.2	10^{11}	10^4	0.247/0.23	[69]	2020
Cs_2SnI_6	Solution/thin film	6	2×10^9	N/A	N/A	[70]	2020
$AG_3Bi_2I_9$	Thremal evaporation/bulk crystal	14.8	8.8×10^{10}	25	0.152/0.187	[71]	2020
$Cs_3Sb_2I_9$	CVD/nanoplate	40	1.26×10^{11}	10^4	0.096/0.058	This work	

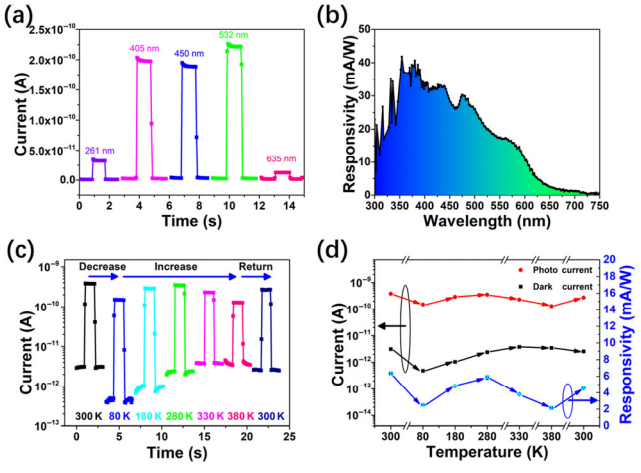

Figure 5 (a) Room temperature spectral photocurrent and (b) responsivity of the $Cs_3Sb_2I_9$ microplate device. (c) Temperature dependent photoresponse and (d) responsivity of the device with the incident wavelength of 532 nm. The measurements were performed under 1 V bias with an incident power density of 20 mW/cm^2.

temperature range of 80 to 380 K under 1 V bias with an incident photon wavelength of 532 nm and a power density of 20 mW/cm^2. As displayed in Figs. 5(c) and 5(d), both the photo- and dark-current reduce with decreasing temperatures. The photocurrent decreases from 379 pA at 300 K to 150 pA at 80 K, while the dark current shows the same tendency from 3 pA to 0.4 pA. Such decreases in currents may be associated with the restricted ion migration at low temperatures. Obviously, the decrease rate of the dark current is slightly faster than that of the photocurrent, resulting in an enhancement of on/off current ratio. In fact, as the temperature goes from 80 to 280 K, the conductance of $Cs_3Sb_2I_9$ microplates increases. Thus, both photo- and dark-current exhibit the positive correlation with operating temperature. However, with increasing temperatures above 280 K, the photocurrent decreases again, while the dark current remains relatively stable. This behavior is different from the previously reported results in lead-based perovskites which showed that both photo- and dark-current rise rapidly with increasing temperatures [72]. This may be the effect of the large exciton binding energy of $Cs_3Sb_2I_9$ microplates, which can effectively maintain their carriers at high temperatures. Moreover, the reproducibility of the on/off switching of the device was also measured in the temperature range of 80 and 380 K and the device demonstrates excellent repeatability and invariable photoresponse to the incident irradiation (Fig. S13 in the ESM). Temperature cycling study shows that the photocurrent and responsivity can recover to more than 70% of their initial values after heating up to 380 K and then cooling back down to room temperature. This indicates that the device has enhanced high tolerance to both low and high temperatures (Fig. 5(d)). The long-term stability of $Cs_3Sb_2I_9$ microplate photodetectors was further evaluated by retesting the devices after they were stored for 100 days in ambient air and moisture. We notice that the dark current of the device gradually increases from 10^{-11} to 10^{-10} A, while the photocurrent decreases slightly as well (Fig. S14 in the ESM). In any case, the device still maintains an on/off current ratio of 100 with the corresponding responsivity of 9.7 mA/W, which is ~ 85% of its initial value.

3 Conclusion

In summary, we have successfully synthesized crystalline, all-inorganic and Pb-free $Cs_3Sb_2I_9$ perovskite microplates using a two-step CVD approach. The obtained microplates show a large stokes shift of 520 meV, a large exciton binding energy of 282 meV and an improved electron-phonon coupling. When these microplates are configured into photoconductive devices, they exhibit a respectable responsivity up to 40 mA/W and detectivity reaching 10^{11} Jones at 532 nm irradiation wavelength. Notably, benefiting from the excellent crystalline quality of microplates, the photodetectors achieve ultra-fast photoresponse with rise and decay time constants as low as 96 μs and 58 μs, respectively. More importantly, due to the enhanced exciton binding energy, the photodetectors also exhibit superior stability under both low and high temperatures. Our findings on the materials properties and photodetector performance strongly suggest that $Cs_3Sb_2I_9$ is an all-inorganic Pb-free perovskite material which will have huge application potentials for photodetectors and other optoelectronic devices.

4 Methods

4.1 Synthesis of $Cs_3Sb_2I_9$ microplates

The $Cs_3Sb_2I_9$ microplates were grown in a single-zone horizontal tube furnace by a two-step CVD approach. Before the experiment, the sapphire or SiO_2 coated Si substrates

were ultrasonically cleaned in acetone, ethanol, and deionized water for 15 minutes each at room temperature, respectively. The substrates were dried initially using a nitrogen drier and then on a hot plate at 60°C for 30 min. In step-I, commercial CsI powder (99.9 %, metal basis, Sigma-Aldrich) was put in an alumina boat, which was placed at the center of the tube furnace heated up to 550 °C with an optimized pressure of 2 Torr for a holding time of 10 min. High-purity argon (99.995%) was used as the carrier gas at a flow rate of 200 sccm to transport the reactant vapor to the downstream of the quartz tube. The substrates were kept in the downstream side of the furnace. The distance between the source boat and substrate was 25 cm. In step-II, commercial SbI_3 powder (98%, Sigma-Aldrich) was deposited at a controlled temperature of 130 °C under 25 sccm of Ar flow, while the pressure and holding time remained the same as step-I. After each step, the furnace was cooled naturally under a continuous Ar flow. Prior to heating, the tube was evacuated to 5 mTorr with a mechanical pump. Next, Ar was injected into the tube for 30 min for flushing to minimize oxygen and moisture before ramping up the temperature. The as-grown samples were then annealed at 180 °C for 15 min inside the N_2 gas-filled tube furnace at atmospheric pressure to obtain $Cs_3Sb_2I_9$ perovskite microplates. The CsI and SbI_3 powders were used in a molar ratio of 1:3 to achieve a proper stoichiometric composition in these two steps. The growth process of $Cs_3Sb_2I_9$ mainly occurs at step-III (annealing process). It just contains melting and mixing of raw materials and recrystallizing of $Cs_3Sb_2I_9$, resulting in the final $Cs_3Sb_2I_9$ microplates, rather than epitaxial growth on the substrates. Therefore, the substrates have no significant impact on the growth results.

4.2 Fabrication of photodetectors

The substrates with prepared $Cs_3Sb_2I_9$ perovskite microplates were first fixed on a sample holder. Then, commercial Ni grids (Structure Probe, Inc., 300 mesh, with the square voids of 70 μm side length) were aimed and put on the substrates under a optical microscope. Au electrodes, with the thickness of 40–50 nm, were next thermally evaporated onto the sample. After removing the Ni grids, square-shaped electrodes with 10 μm apart were already formed on the microplates.

4.3 Characterization

XRD characterization was performed on a Bruker D2 system using Cu-Kα radiation. High-resolution XRD and corresponding rocking cuve were recorded by a Rigaku SmartLab X-ray diffractometer. The morphology and elemental composition of the sample were studied by a field-emission scanning electron microscope (FESEM, Philips XL30 FEG) equipped with energy-dispersive X-ray spectroscopy (EDX) capability. High-resolution transmission electron microscopy (HRTEM) image of the sample were obtained by a Tecnai G2 F20 S-TWIN microscope. Optical absorption measurements were conducted by a PerkinElmer Lambda 2S UV-vis spectrophotometer. Room temperature photoluminescence (PL) and mappings of $Cs_3Sb_2I_9$ microplates were performed by an WITec alpha300 R microscope with a 532 nm laser as the excitation sourse. Time-resolved PL spectra was obtained on an Edinburgh FLS 920 fluorescence spectrometer. The valence band spectrum was obtained by Ultraviolet-Ambient Pressure Photoemission Spectroscopy (UV-APS). Measurements were conducted using a KP technology (APS04) instrument in a N_2-filled APS module. Hall mobility, conduction type and carrier density of material were recorded by a Hall effect measurement system (Ecopia HMS-5300). All the photodetector measurements were performed by using a standard probe station with an Agilent 4155C semiconductor analyzer coupled with lasers (261, 405, 450, 532, 650 nm) as the light source, whose power was measured by a Thorlabs PM400 power meter. The response times were evaluated by using an optical chopper (Sanford, SR540) to turn on and turn off the light that illuminated on the device. Also, a low noise current amplifier (Stanford, SR570) combined with a digital oscillator (Tektronix TBS 1102B EDU) were used to record the time and corresponding photocurrent values.

Acknowledgements

This work was supported by the National Natural Science Foundation of China (Nos. 11874351, 11874352, 51672229, and 61805237), the Hong Kong Scholars Program (No. XJ2019027), the General Research Fund (CityU 11204618) and the Theme-based Research (No. T42-103/16-N) of the Research Grants Council of Hong Kong SAR, China, CityU SGP-9380076 and the Foshan Innovative and Entrepreneurial Research Team Program (No. 2018IT100031).

Electronic Supplementary Material: Supplementary material (crystallographic data and 2D layered structure of the $Cs_3Sb_2I_9$ perovskite; SEM, AFM and EDX spectrum of $Cs_3Sb_2I_9$ microplates; Tauc plot of the absorption spectrum and 3D PL mapping of an individual microplate; TRPL spectrum of the microplates; the reproducible on/off switching of the device under 0.5 V bias and at different temperatures from 80 to 380 K; the reproducible on/off switching of the device measured after 100 days) is available in the online version of this article at https://doi.org/10.1007/s12274-021-3351-x.

References

[1] Li, L.; Chen, H. Y.; Fang, Z. M.; Meng, X. Y.; Zuo, C. T.; Lv, M. L.; Tian, Y. Z.; Fang, Y.; Xiao, Z.; Shan, C. X. et al. An electrically modulated single-color/dual-color imaging photodetector. *Adv. Mater.* **2020**, *32*, 1907257.

[2] Chen, H. Y.; Liu, H.; Zhang, Z. M.; Hu, K.; Fang, X. S. Nanostructured photodetectors: From ultraviolet to terahertz. *Adv. Mater.* **2016**, *28*, 403–433.

[3] Xu, Y. L.; Lin, Q. Q. Photodetectors based on solution-processable semiconductors: Recent advances and perspectives. *Appl. Phys. Rev.* **2020**, *7*, 011315.

[4] Zhou, Q. T.; Park, J. G.; Nie, R. M.; Thokchom, A. K.; Ha, D.; Pan, J.; Seok, S. I.; Kim, T. Nanochannel-assisted perovskite nanowires: From growth mechanisms to photodetector applications. *ACS Nano* **2018**, *12*, 8406–8414.

[5] Yang, B.; Li, Y. J.; Tang, Y. X.; Mao, X.; Luo, C.; Wang, M. S.; Deng, W. Q.; Han, K. L. Constructing sensitive and fast lead-free single-crystalline perovskite photodetectors. *J. Phys. Chem. Lett.* **2018**, *9*, 3087–3092.

[6] Hu, X.; Zhang, X. D.; Liang, L.; Bao, J.; Li, S.; Yang, W.; Xie, Y. High-performance flexible broadband photodetector based on organolead halide perovskite. *Adv. Funct. Mater.* **2014**, *24*, 7373–7380.

[7] Dou, L. T.; Yang, Y. M.; You, J. B.; Hong, Z. R.; Chang, W. H.; Li, G.; Yang, Y. Solution-processed hybrid perovskite photodetectors with high detectivity. *Nat. Commun.* **2014**, *5*, 5404.

[8] Liu, J. Y.; Xue, Y. Z.; Wang, Z. Y.; Xu, Z. Q.; Zheng, C. X.; Weber, B.; Song, J. C.; Wang, Y. S.; Lu, Y. R.; Zhang, Y. P. et al. Two-dimensional $CH_3NH_3PbI_3$ perovskite: Synthesis and optoelectronic application. *ACS Nano* **2016**, *10*, 3536–3542.

[9] Shi, D.; Adinolfi, V.; Comin, R.; Yuan, M. J.; Alarousu, E.; Buin, A.; Chen, Y.; Hoogland, S.; Rothenberger, A.; Katsiev, K. et al. Low trap-state density and long carrier diffusion in organolead trihalide perovskite single crystals. *Science* **2015**, *347*, 519–522.

[10] Wang, K.; Li, Z. Z.; Zhou, F. G.; Wang, H. R.; Bian, H.; Zhang, H.; Wang, Q.; Jin, Z. W.; Ding, L. M.; Liu, S. Ruddlesden–popper 2D

component to stabilize γ-$CsPbI_3$ perovskite phase for stable and efficient photovoltaics. *Adv. Energy Mater.* **2019**, *9*, 1902529.

[11] Wang, H. R.; Bian, H.; Jin, Z. W.; Zhang, H.; Liang, L.; Wen, J. L.; Wang, Q.; Ding, L. M.; Liu, S. F. Cesium lead mixed-halide perovskites for low-energy loss solar cells with efficiency beyond 17%. *Chem. Mater.* **2019**, *31*, 6231–6238.

[12] Li, Z. Z.; Zhou, F. G.; Wang, Q.; Ding, L. M.; Jin, Z. W. Approaches for thermodynamically stabilized $CsPbI_3$ solar cells. *Nano Energy* **2020**, *71*, 104634.

[13] Bian, H.; Wang, H. R.; Li, Z. Z.; Zhou, F. G.; Xu, Y. K.; Zhang, H.; Wang, Q.; Ding, L. M.; Liu, S. F.; Jin, Z. W. Unveiling the effects of hydrolysis-derived DMAI/$DMAPbI_x$ intermediate compound on the performance of $CsPbI_3$ solar cells. *Adv. Sci.* **2020**, *7*, 1902868.

[14] Wang, F.; Mei, J. J.; Wang, Y. P.; Zhang, L. G.; Zhao, H. F.; Zhao, D. X. Fast photoconductive responses in organometal halide perovskite photodetectors. *ACS Appl. Mater. Interfaces* **2016**, *8*, 2840–2846.

[15] Juarez-Perez, E. J.; Hawash, Z.; Raga, S. R.; Ono, L. K.; Qi, Y. B. Thermal degradation of $CH_3NH_3PbI_3$ perovskite into NH_3 and CH_3I gases observed by coupled thermogravimetry–mass spectrometry analysis. *Energy Environ. Sci.* **2016**, *9*, 3406–3410.

[16] Conings, B.; Drijkoningen, J.; Gauquelin, N.; Babayigit, A.; D'Haen, J.; D'Olieslaeger, L.; Ethirajan, A.; Verbeeck, J.; Manca, J.; Mosconi, E. et al. Intrinsic thermal instability of methylammonium lead trihalide perovskite. *Adv. Energy Mater.* **2015**, *5*, 1500477.

[17] Yang, J. L.; Siempelkamp, B. D.; Liu, D. Y.; Kelly, T. L. Investigation of $CH_3NH_3PbI_3$ degradation rates and mechanisms in controlled humidity environments using *in situ* techniques. *ACS Nano* **2015**, *9*, 1955–1963.

[18] De Roo, J.; Ibáñez, M.; Geiregat, P.; Nedelcu, G.; Walravens, W.; Maes, J.; Martins, J. C.; Van Driessche, I.; Kovalenko, M. V.; Hens, Z. Highly dynamic ligand binding and light absorption coefficient of cesium lead bromide perovskite nanocrystals. *ACS Nano* **2016**, *10*, 2071–2081.

[19] Akkerman, Q. A.; D'Innocenzo, V.; Accornero, S.; Scarpellini, A.; Petrozza, A.; Prato, M.; Manna, L. Tuning the optical properties of cesium lead halide perovskite nanocrystals by anion exchange reactions. *J. Am. Chem. Soc.* **2015**, *137*, 10276–10281.

[20] Yettapu, G. R.; Talukdar, D.; Sarkar, S.; Swarnkar, A.; Nag, A.; Ghosh, P.; Mandal, P. Terahertz conductivity within colloidal $CsPbBr_3$ perovskite nanocrystals: Remarkably high carrier mobilities and large diffusion lengths. *Nano Lett.* **2016**, *16*, 4838–4848.

[21] Sun, S. B.; Yuan, D.; Xu, Y.; Wang, A. F.; Deng, Z. T. Ligand-mediated synthesis of shape-controlled cesium lead halide perovskite nanocrystals via reprecipitation process at room temperature. *ACS Nano* **2016**, *10*, 3648–3657.

[22] Pradhan, B.; Kumar, G. S.; Sain, S.; Dalui, A.; Ghorai, U. K.; Pradhan, S. K.; Acharya, S. Size tunable cesium antimony chloride perovskite nanowires and nanorods. *Chem. Mater.* **2018**, *30*, 2135–2142.

[23] Tong, X. W.; Kong, W. Y.; Wang, Y. Y.; Zhu, J. M.; Luo, L. B.; Wang, Z. H. High-performance red-light photodetector based on lead-free bismuth halide perovskite film. *ACS Appl. Mater. Interfaces* **2017**, *9*, 18977–18985.

[24] Chen, J.; Luo, Z. Y.; Fu, Y. P.; Wang, X. X.; Czech, K. J.; Shen, S. H.; Guo, L. J.; Wright, J. C.; Pan, A. L.; Jin, S. Tin(IV)-tolerant vapor-phase growth and photophysical properties of aligned cesium tin halide perovskite ($CsSnX_3$; X = Br, I) nanowires. *ACS Energy Lett.* **2019**, *4*, 1045–1052.

[25] Huang, H.; Bodnarchuk, M. I.; Kershaw, S. V.; Kovalenko, M. V.; Rogach, A. L. Lead halide perovskite nanocrystals in the research spotlight: Stability and defect tolerance. *ACS Energy Lett.* **2017**, *2*, 2071–2083.

[26] Hoefler, S. F.; Trimmel, G.; Rath, T. Progress on lead-free metal halide perovskites for photovoltaic applications: A review. *Monatsh. Chem.* **2017**, *148*, 795–826.

[27] Parrott, E. S.; Milot, R. L.; Stergiopoulos, T.; Snaith, H. J.; Johnston, M. B.; Herz, L. M. Effect of structural phase transition on charge-carrier lifetimes and defects in $CH_3NH_3SnI_3$ perovskite. *J. Phys. Chem. Lett.* **2016**, *7*, 1321–1326.

[28] Hao, F.; Stoumpos, C. C.; Cao, D. H.; Chang, R. P. H.; Kanatzidis, M. G. Lead-free solid-state organic–inorganic halide perovskite solar cells. *Nat. Photonics* **2014**, *8*, 489–494.

[29] Noel, N. K.; Stranks, S. D.; Abate, A.; Wehrenfennig, C.; Guarnera, S.; Haghighirad, A. A.; Sadhanala, A.; Eperon, G. E.; Pathak, S. K.; Johnston, M. B. et al. Lead-free organic–inorganic tin halide perovskites for photovoltaic applications. *Energy Environ. Sci.* **2014**, *7*, 3061–3068.

[30] Hebig, J. C.; Kühn, I.; Flohre, J.; Kirchartz, T. Optoelectronic properties of $(CH_3NH_3)_3Sb_2I_9$ thin films for photovoltaic applications. *ACS Energy Lett.* **2016**, *1*, 309–314.

[31] Chatterjee, S.; Pal, A. J. Tin(IV) Substitution in $(CH_3NH_3)_3Sb_2I_9$: Toward low-band-gap defect-ordered hybrid perovskite solar cells. *ACS Appl. Mater. Interfaces* **2018**, *10*, 35194–35205.

[32] Umar, F.; Zhang, J.; Jin, Z. X.; Muhammad, I.; Yang, X. K.; Deng, H.; Jahangeer, K.; Hu, Q. S.; Song, H. S.; Tang, J. Dimensionality controlling of $Cs_3Sb_2I_9$ for efficient all-inorganic planar thin film solar cells by HCl-assisted solution method. *Adv. Opt. Mater.* **2019**, *7*, 1801368.

[33] Zuo, C. T.; Ding, L. M. Lead-free perovskite materials $(NH_4)_3Sb_2I_xBr_{9-x}$. *Angew. Chem., Int. Ed.* **2017**, *56*, 6528–6532.

[34] Ma, Z. Z.; Shi, Z. F.; Yang, D. W.; Zhang, F.; Li, S.; Wang, L. T.; Wu, D.; Zhang, Y. T.; Na, G. R.; Zhang, L. J. et al. Electrically-driven violet light-emitting devices based on highly stable lead-free perovskite $Cs_3Sb_2Br_9$ quantum dots. *ACS Energy Lett.* **2020**, *5*, 385–394.

[35] Zhang, J.; Yang, Y.; Deng, H.; Farooq, U.; Yang, X. K.; Khan, J.; Tang, J.; Song, H. S. High quantum yield blue emission from lead-free inorganic antimony halide perovskite colloidal quantum dots. *ACS Nano* **2017**, *11*, 9294–9302.

[36] Singh, A.; Boopathi, K. M.; Mohapatra, A.; Chen, Y. F.; Li, G.; Chu, C. W. Photovoltaic performance of vapor-assisted solution-processed layer polymorph of $Cs_3Sb_2I_9$. *ACS Appl. Mater. Interfaces* **2018**, *10*, 2566–2573.

[37] Correa-Baena, J. P.; Nienhaus, L.; Kurchin, R. C.; Shin, S. S.; Wieghold, S.; Hartono, N. T. P.; Layurova, M.; Klein, N. D.; Poindexter, J. R.; Polizzotti, A. et al. *A*-site cation in inorganic $A_3Sb_2I_9$ perovskite influences structural dimensionality, exciton binding energy, and solar cell performance. *Chem. Mater.* **2018**, *30*, 3734–3742.

[38] Park, B. W.; Philippe, B.; Zhang, X. L.; Rensmo, H.; Boschloo, G.; Johansson, E. M. J. Bismuth based hybrid perovskites $A_3Bi_2I_9$ (A: Methylammonium or cesium) for solar cell application. *Adv. Mater.* **2015**, *27*, 6806–6813.

[39] Li, J.; Luo, L. H.; Huang, H. W.; Ma, C.; Ye, Z. Z.; Zeng, J.; He, H. P. 2D behaviors of excitons in cesium lead halide perovskite nano-platelets. *J. Phys. Chem. Lett.* **2017**, *8*, 1161–1168.

[40] Yang, Z.; Wang, M. Q.; Qiu, H. W.; Yao, X.; Lao, X. Z.; Xu, S. J.; Lin, Z. H.; Sun, L. Y.; Shao, J. Y. Engineering the exciton dissociation in quantum-confined 2D $CsPbBr_3$ nanosheet films. *Adv. Funct. Mater.* **2018**, *28*, 1705908.

[41] Jain, S. M.; Phuyal, D.; Davies, M. L.; Li, M.; Philippe, B.; De Castro, C.; Qiu, Z.; Kim, J.; Watson, T.; Tsoi, W. C. et al. An effective approach of vapour assisted morphological tailoring for reducing metal defect sites in lead-free, $(CH_3NH_3)_3Bi_2I_9$ bismuth-based perovskite solar cells for improved performance and long-term stability. *Nano Energy* **2018**, *49*, 614–624.

[42] Yang, B.; Yin, L. X.; Niu, G. D.; Yuan, J. H.; Xue, K. H.; Tan, Z. F.; Miao, X. S.; Niu, M.; Du, X. Y.; Song, H. S. et al. Lead-free halide Rb_2CuBr_3 as sensitive X-Ray scintillator. *Adv. Mater.* **2019**, *31*, 1904711.

[43] Liu, M.; Zhong, G. H.; Yin, Y. M.; Miao, J. S.; Li, K.; Wang, C. Q.; Xu, X. R.; Shen, C.; Meng, H. Aluminum-doped cesium lead bromide perovskite nanocrystals with stable blue photoluminescence used for display backlight. *Adv. Sci.* **2017**, *4*, 1700335.

[44] Swarnkar, A.; Chulliyil, R.; Ravi, V. K.; Irfanullah, M.; Chowdhury, A.; Nag, A. Colloidal $CsPbBr_3$ perovskite nanocrystals: Luminescence beyond traditional quantum dots. *Angew. Chem., Int. Ed.* **2015**, *54*, 15424–15428.

[45] Jun, T.; Sim, K.; Iimura, S.; Sasase, M.; Kamioka, H.; Kim, J.; Hosono, H. Lead-free highly efficient blue-emitting $Cs_3Cu_2I_5$ with 0D electronic structure. *Adv. Mater.* **2018**, *30*, 1804547.

[46] Lian, L. Y.; Zheng, M. Y.; Zhang, W. Z.; Yin, L. X.; Du, X. Y.; Zhang, P.; Zhang, X. W.; Gao, J. B.; Zhang, D. L.; Gao, L. et al. Efficient and reabsorption-free radioluminescence in $Cs_3Cu_2I_5$ nanocrystals with self-trapped excitons. *Adv. Sci.* **2020**, *7*, 2000195.

[47] Ma, Z. Z.; Shi, Z. F.; Qin, C. C.; Cui, M. H.; Yang, D. W.; Wang, X. J.; Wang, L. T.; Ji, X. Z.; Chen, X.; Sun, J. L. et al. Stable yellow light-emitting devices based on ternary copper halides with broadband emissive self-trapped excitons. *ACS Nano* **2020**, *14*, 4475–4486.

[48] Li, Y.; Shi, Z. F.; Wang, L. T.; Chen, Y. C.; Liang, W. Q.; Wu, D.; Li, X. J.; Zhang, Y.; Shan, C. X.; Fang, X. S. Solution-processed one-dimensional $CsCu_2I_3$ nanowires for polarization-sensitive and flexible ultraviolet photodetectors. *Mater. Horiz.* **2020**, *7*, 1613–1622.

[49] Xie, B. M.; Xie, R. H.; Zhang, K.; Yin, Q. W.; Hu, Z. C.; Yu, G.; Huang, F.; Cao, Y. Self-filtering narrowband high performance organic photodetectors enabled by manipulating localized Frenkel exciton dissociation. *Nat. Commun.* **2020**, *11*, 2871.

[50] Gong, Y. P.; Liu, Q. F.; Gong, M. G.; Wang, T.; Zeng, G. G.; Chan, W. L.; Wu, J. High-performance photodetectors based on effective exciton dissociation in protein-adsorbed multiwalled carbon nanotube nanohybrids. *Adv. Opt. Mater.* **2017**, *5*, 1600478.

[51] McCall, K. M.; Stoumpos, C. C.; Kostina, S. S.; Kanatzidis, M. G.; Wessels, B. W. Strong electron–phonon coupling and self-trapped excitons in the defect halide perovskites $A_3M_2I_9$ (A = Cs, Rb; M = Bi, Sb). *Chem. Mater.* **2017**, *29*, 4129–4145.

[52] Toyozawa, Y. Further contribution to the theory of the line-shape of the exciton absorption band. *Prog. Theor. Phys.* **1962**, *27*, 89–104.

[53] Dawson, K. R; Pooley, D. F band absorption in alkali halides as a function of temperature. *Phys. Status Solidi B* **1969**, *35*, 95–105.

[54] Leung, C. H.; Song, K. S. On the luminescence quenching of *F* centres in alkali halides. *Solid State Commun.* **1980**, *33*, 907–910.

[55] Urbach, F. The long-wavelength edge of photographic sensitivity and of the electronic absorption of solids. *Phys. Rev.* **1953**, *92*, 1324.

[56] Masada, S.; Yamada, T.; Tahara, H.; Hirori, H.; Saruyama, M.; Kawawaki, T.; Sato, R.; Teranishi, T.; Kanemitsu, Y. Effect of a-site cation on photoluminescence spectra of single lead bromide perovskite nanocrystals. *Nano Lett.* **2020**, *20*, 4022–4028.

[57] Van Roosbroeck, W.; Shockley, W. Photon-radiative recombination of electrons and holes in germanium. *Phys. Rev.* **1954**, *94*, 1558–1560.

[58] Olson, C. G.; Lynch, D. W. Longitudinal-optical-phonon-plasmon coupling in GaAs. *Phys. Rev.* **1969**, *177*, 1231–1234.

[59] Konstantatos, G.; Clifford, J.; Levina, L.; Sargent, E. H. Sensitive solution-processed visible-wavelength photodetectors. *Nat. Photon.* **2007**, *1*, 531–534.

[60] Liu, Y. C.; Zhang, Y. X.; Yang, Z.; Ye, H. C.; Feng, J. S.; Xu, Z.; Zhang, X.; Munir, R.; Liu, J.; Zuo, P. et al. Multi-inch single-crystalline perovskite membrane for high-detectivity flexible photosensors. *Nat. Commun.* **2018**, *9*, 5302.

[61] Waleed, A.; Tavakoli, M. M.; Gu, L. L.; Wang, Z. Y.; Zhang, D. Q.; Manikandan, A.; Zhang, Q. P.; Zhang, R. J.; Chueh, Y. L.; Fan, Z. Y. Lead-free perovskite nanowire array photodetectors with drastically improved stability in nanoengineering templates. *Nano Lett.* **2017**, *17*, 523–530.

[62] Ji, C. M.; Wang, P.; Wu, Z. Y.; Sun, Z. H.; Li, L. N.; Zhang, J.; Hu, W. D.; Hong, M. C.; Luo, J. H. Inch-size single crystal of a lead-free organic-inorganic hybrid perovskite for high-performance photodetector. *Adv. Funct. Mater.* **2018**, *28*, 1705467.

[63] Lei, L. Z.; Shi, Z. F.; Li, Y.; Ma, Z. Z.; Zhang, F.; Xu, T. T.; Tian, Y. T.; Wu, D.; Li, X. J.; Du, G. T. High-efficiency and air-stable photodetectors based on lead-free double perovskite $Cs_2AgBiBr_6$ thin films. *J. Mater. Chem. C* **2018**, *6*, 7982–7988.

[64] Zhou, J.; Luo, J. J.; Rong, X. M.; Wei, P. J.; Molokeev, M. S.; Huang, Y.; Zhao, J.; Liu, Q. L.; Zhang, X. W.; Tang, J. *et al*. Lead-free perovskite derivative $Cs_2SnCl_{6-x}Br_x$ single crystals for narrowband photodetectors. *Adv. Opt. Mater.* **2019**, *7*, 1900139.

[65] Zhang, Z. X.; Li, C.; Lu, Y.; Tong, X. W.; Liang, F. X.; Zhao, X. Y.; Wu, D.; Xie, C.; Luo, L. B. Sensitive deep ultraviolet photodetector and image sensor composed of inorganic lead-free $Cs_3Cu_2I_5$ perovskite with wide bandgap. *J. Phys. Chem. Lett.* **2019**, *10*, 5343–5350.

[66] Fang, C.; Wang, H. Z.; Shen, Z. X.; Shen, H. Z.; Wang, S.; Ma, J. Q.; Wang, J.; Luo, H. M.; Li, D. H. High-performance photodetectors based on lead-free 2D ruddlesden-popper perovskite/MoS_2 hetero-structures. *ACS Appl. Mater. Interfaces* **2019**, *11*, 8419–8427.

[67] Li, Y.; Shi, Z. F.; Lei, L. Z.; Li, S.; Yang, D. W.; Wu, D.; Xu, T. T.; Tian, Y. Z.; Lu, Y. J.; Wang, Y. et al. Ultrastable lead-free double perovskite photodetectors with imaging capability. *Adv. Mater. Interfaces* **2019**, *6*, 1900188.

[68] Zheng, Z.; Hu, Q. S.; Zhou, H. Z.; Luo, P.; Nie, A. M.; Zhu, H. M.; Gan, L.; Zhuge, F. W.; Ma, Y.; Song, H. S. et al. Submillimeter and lead-free $Cs_3Sb_2Br_9$ perovskite nanoflakes: Inverse temperature crystallization growth and application for ultrasensitive photodetectors. *Nanoscale Horiz.* **2019**, *4*, 1372–1379.

[69] Li, W. G.; Wang, X. D.; Liao, J. F.; Jiang, Y.; Kuang, D. B. Enhanced on–off ratio photodetectors based on lead-free $Cs_3Bi_2I_9$ single crystal thin films. *Adv. Funct. Mater.* **2020**, *30*, 1909701.

[70] Krishnaiah, M.; Khan, M. I.; Kumar, A.; Jin, S. H. Impact of CsI concentration, relative humidity, and annealing temperature on lead-free Cs_2SnI_6 perovskites: Toward visible light photodetectors application. *Mater. Lett.* **2020**, *269*, 127675.

[71] Zhang, W. C.; Sui, Y.; Kou, B.; Peng, Y.; Wu, Z. Y.; Luo, J. H. Large-area exfoliated lead-free perovskite-derivative single-crystalline membrane for flexible low-defect photodetectors. *ACS Appl. Mater. Interfaces* **2020**, *12*, 9141–9149.

[72] Tian, C. C.; Wang, F.; Wang, Y. P.; Yang, Z.; Chen, X. J.; Mei, J. J.; Liu, H. Z.; Zhao, D. X. Chemical vapor deposition method grown all-inorganic perovskite microcrystals for self-powered photodetectors. *ACS Appl. Mater. Interfaces* **2019**, *11*, 15804–15812.